Optimal cell tab design and cooling strategy for cylindrical lithium-ion batteries

Shen Li[a, *], Niall Kirkaldy[a], Cheng Zhang[b], Krishnakumar Gopalakrishnan[c], Tazdin Amietszajew[b], Laura Bravo Diaz[a], Jorge Varela Barreras[a], Mosayeb Shams[a], Xiao Hua[a], Yatish Patel[a, d], Gregory J. Offer[a, d], Monica Marinescu[a, d]

* Corresponding author.
E-mail address: lishensean@gmail.com (S. Li).

Affiliations:

a. **Department of Mechanical Engineering, Imperial College London, London SW7 2AZ, United Kingdom**
b. **Institute for Future Transport and Cities, Coventry University, Coventry CV1 5FB, United Kingdom**
c. **The Centre for Computational Science (CCS), 131 Christopher Ingold Building, University College London, London WC1H 0AJ, United Kingdom**
d. **The Faraday Institution, Harwell Science and Innovation Campus, Didcot OX11 0RA, United Kingdom**

Abstract

The ability to correctly predict the behavior of lithium ion batteries is critical for safety, performance, cost and lifetime. Particularly important for this purpose is the prediction of the internal temperature of cells, because of the positive feedback between heat generation and current distribution. In this work, a comprehensive electro-thermal model is developed for a cylindrical lithium-ion cell. The model is comprehensively parameterized and validated with experimental data for 2170 cylindrical cells (LG M50T, NMC811), including direct core temperature measurements. The validated model is

used to study different cell designs and cooling approaches and their effects on the internal temperature of the cell. Increasing the number of tabs connecting the jellyroll to the base of the cylindrical can reduce the internal thermal gradient by up to 25.41%. On its own, side cooling is more effective than base cooling at removing heat, yet both result in thermal gradients within the can of a similar magnitude, irrespective of the number of cell tabs. The results are of immediate interest to both cell manufacturers and battery pack designers, while the modelling and parameterization framework created is an essential tool for energy storage system design.

Keywords: Lithium-ion battery; Electro-thermal model; Cell design; Thermal management

1 Introduction

The global stock of electric vehicles (EVs) increased from just under 1 million in 2014 to around 7.2 million in 2019, and is forecasted to reach 116 million by 2030 [1,2]. The rapid growth of this industry has been linked to a significant reduction in the cost of lithium-ion batteries (LIBs) over the past decade [2]. However, to further reduce both the economic and environmental costs associated with LIBs, their performance and lifetime must be further improved [3].

Temperature is a key factor in the performance, lifetime and safety of cells [4–7]. For example, one study showed every degree of temperature rise shortens the lifetime of lithium-ion battery by 2 months over 30-40 °C [8]. Active cooling with a Thermal Management System (TMS) is usually required to ensure a battery pack operates within a suitable temperature range. However, due to heat transfer limitations, thermal gradients still exist between cells and within a single cell, especially during aggressive discharge or fast charging events, reducing the useable pack capacity and lifespan [9,10]. These adverse effects are caused or exacerbated by inhomogeneities in a) degradation [11], b) lithium concentration [7], c) current density [13], d) mechanical stress [14], e) microstructure [15], and f) chemical reactions [16].

Two thermal factors influence significantly the overall performance of a cell – a) the thermal boundary conditions, such as given by the choice of TMS [10] and b) the internal heat generation and transport, influenced by the cell design [17]. Studies on TMS design include configuration of air flow [18] and cooling plate [19], cooling factors sensitivity [20], cell spacing [21] and cell temperature imaging [22]. A distributed

two-dimensional pouch cell model has demonstrated that tab cooling results in a more uniform temperature gradient than surface cooling, albeit at the expense of a higher average cell temperature [23]. In the majority of cylindrical cell models that reveal the effects of electrochemical and thermal inhomogeneities [11,24,25], thermal boundary conditions are applied directly on jellyroll surfaces, while the contacts with the metal can are neglected. Recent thermal analysis indicates that the metal can has a significant influence on thermal gradients [26]. A comprehensive model that takes into account all geometrical components is needed for accurately predicting cylindrical cell electro-thermal behaviors.

Aside from the thermal boundary conditions, the internal cell design, such as the number and position of tabs, also plays an important role in the cell thermal behavior [17,27]. For cylindrical cells, prior simulation study [25] and experimental work [17] have shown that using more tabs leads to lower temperature rise and thermal gradients. Recently, Tesla Inc. has filed a patent on the fabrication of cylindrical cells employing a novel 'continuous tab' design, expected to significantly improve the cell's performance through reduced heat generation [28].

To quantitatively study the effects of both cooling choice and cell design, a cell-level distributed model is needed, which can accommodate for temperature gradients within a cell, and their effects on local state of charge. There are two broad categories of models that could, in principle, serve as a basis for such a study: continuum models and equivalent circuit models. A cell-level pseudo two-dimensional (P2D) physics-based model [29–32] is computationally intensive. However, derived from the

P2D model, various Multi-Scale Multi-Dimensional (MSMD) models have been proposed to accelerate the simulation from electrochemical sub-domains up to the cell level [24,25,33–37]. Newman, Tiedemann, Gu and Kwon (NTGK) et al. [38–41] pioneered a semi-empirical model which has elucidated many aspects of cell behavior at the cell scale [42–44]. These types of models are notoriously difficult to parameterize with confidence, so they cannot be easily adaptable to different cells [45].

Owing to its ease of parameterization and low computational cost, the Equivalent Circuit Network (ECN) is an empirical type model and has been widely adapted for pouch cells [45,46]. For instance, a 2D electro-thermal ECN model with particular consideration of thermal boundaries was developed for pouch cells [23,27]. However, to the best of our knowledge, there hasn't been studies developing reduced order models that take into account the structure of cylindrical cells.

Here we introduce a distributed electro-thermal coupled ECN model for a cylindrical cell. Importantly, this is the first cylindrical cell model to include the physical aspects of the cell structure and geometry, including the metal can, and the number and position of tabs. The model is flexible, allowing the user to vary with ease discretization, number of ECN branches and cell components. The proposed electro-thermal model is validated against experimental data from LG M50T cylindrical cells instrumented with a thermocouple placed in the core. These cells are relevant for automotive applications, as they contain the C/Si-NMC811 chemistry, and have the larger 2170 form factor. The validated model serves as the basis for a comprehensive evaluation of thermal management strategies, and helps identify the optimal combination of cooling schemes and cell

tab design. A new metric named ‘average function value’ is proposed to compare the efficiency of different thermal management strategies, by taking into account the cell cooling rate and the cell internal thermal gradients.

2 Model description

The cell-level distributed model is composed of coupled electrical and thermal domains and is implemented using an ECN framework in Python 3.7. Given the initial and boundary conditions, it describes a temporal and spatial evolution of various variables of interest, such as current density and temperature within the cylindrical cell.

Fig. 1 shows a schematic of the distributed model. A cylindrical jellyroll, consisting of interleaved electrode and separator layers, forms the computational domain, and is encapsulated by a metal can connected to external current-conducting tabs. The jellyroll core area is filled with separator and hollow space for the LG M50T cell according to the disassembly result shown in **Fig. 2**(b). The angular direction of the jellyroll is chosen as the x-axis. Any position on the spiral can be calculated via the Archimedes spiral equation. The axial and radial directions of the jellyroll correspond to the y and z axes respectively. The computational domain is discretized into multiple unit volumes; within each volume, all the constituent components (anodes, cathodes, separators and current collectors) are arranged in a stacked configuration. An ECN describes the electrical and thermal behavior within each element.

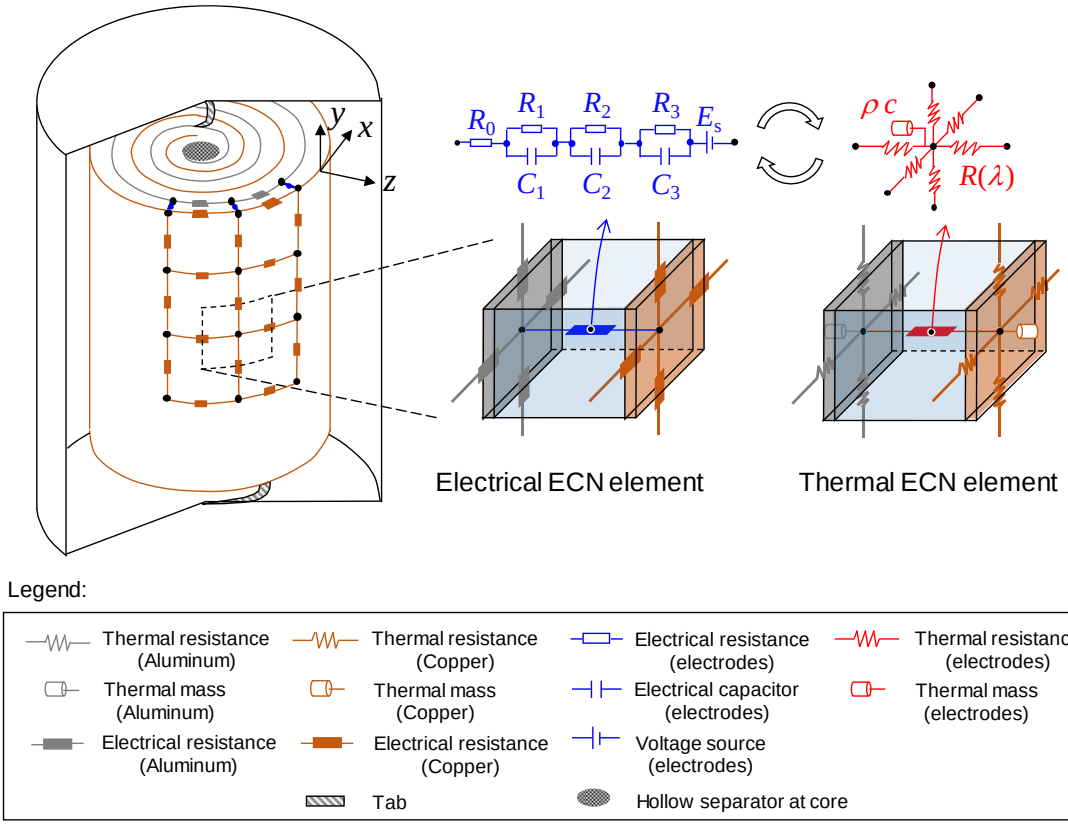


Fig. 1. Schematic representation of the cell-level model. Left: Cylindrical cell geometry containing jellyroll, tab and can. Middle: electrical model element containing electrode pair (anode, separator and cathode) and current collector components. Right: thermal model element containing electrode and current collector components.

2.1 Three-dimensional electrical ECN model

The conventional ECN model is adopted to describe the local electrical state, *i.e.* State of Charge (SoC) and resistances, with ECN models distributed over the jellyroll to capture inhomogeneities in electrical states. As shown in **Fig. 1**, the local ECN includes a voltage source E_s representing the Open Circuit Voltage (OCV), a series resistance R_0 representing the instantaneous ohmic resistance, and a set of Resistor-Capacitor (RC) branches, R_i and C_i that capture the transient response. To capture a wide range of time scales in the electrochemical response, three RC pairs are used for

the results illustrated here.

According to Kirchhoff's voltage law [47], the terminal voltage $\Delta\phi^{\mathrm{El}}$ of the electrode pair unit is given by:

$$\Delta\phi^{\mathrm{El}} = E_{\mathrm{s}} - \sum_{i=1}^{3} R_i I_i - R_0 I\,, \tag{1}$$

where I_i is the branch current in the resistor R_i and I is the current in resistor R_0. For the current collector components charge balance conservation [47] is considered only in the *x* and *y* axes, because the current collectors thickness is negligible relative to the spiral length:

$$\sigma\nabla\cdot(\nabla\phi^{\mathrm{CC}}) = \sigma\frac{\partial^2\phi^{\mathrm{CC}}}{\partial x^2} + \sigma\frac{\partial^2\phi^{\mathrm{CC}}}{\partial y^2} = 0\,, \tag{2}$$

where σ is the conductivity of the current collector and ϕ^{CC} its local potential. The circuit components of the electrical model, the resistances, capacitances and voltage source are functions of the cell's SoC and temperature.

2.2 Three-dimensional thermal ECN model

The thermal model consists of heat transfer and heat source terms. As shown in **Fig. 1**, within each thermal element heat conduction along the *x*, *y* and *z* directions is modelled by thermal resistances R (or local heat transfer coefficients λ). In the thermal ECN the anode, cathode and separator are lumped into one bulk material (electrode pair) in the thermal ECN. This approximation is valid in the heat transfer process because their thermal conduction coefficients are similar and significantly smaller than that of the current collectors (see **Table I)**. The heat transfer equation [48] for the electrode pair, and current collector materials are given by:

$$\rho c \frac{\partial T}{\partial t} = \lambda_x \frac{\partial^2 T}{\partial x^2} + \lambda_y \frac{\partial^2 T}{\partial y^2} + \lambda_z \frac{\partial^2 T}{\partial z^2} + q\,, \tag{3}$$

where ρ, c, λ and are the mass density, heat capacity, heat transfer coefficient and temperature of the material (electrodes pair, current collector or metal can). λ_x, λ_y and λ_z are the corresponding heat transfer coefficients in the three directions, and q is the heat source.

The heat transfer between the jellyroll and the metal can is included, as it has been shown to impact thermal results [26]. In the LG M50T cells used here, the outside layer of the jellyroll spiral is wrapped by 5 layers of separator according to disassembly result, which in turn is in contact with the inside layer of the metal can. The jellyroll core is occupied by hollow separator as seen in **Fig. 2**(a). In the thermal model, volume-averaged (reduced) heat capacity of separator is applied on the core element standing for the core area. The core element allows heat exchange with surrounding aluminum unit volumes in radial direction. At the bottom of the jellyroll, only the separator edge (with low thermal conductivity) is in touch with the bottom of the metal can, as the separator is longer than the current collectors and electrodes, as seen in **Fig. 2**(b). There is a gap between the top of the jellyroll and the metal can inside surface. Owing to the above geometrical facts, in the thermal model the top and bottom surfaces of the jellyroll are thermally connected to the metal can only through the positive and negative tab, respectively.

The thermal boundary condition is applied on the metal can. A convection boundary condition [48] is imposed as:

$$Q_{\text{conv}} = h(T - T_{\text{ambient}})\,, \tag{4}$$

where Q_{conv} is the heat transferred due to convection, h is convective heat transfer coefficient, T is the temperature at the boundary and T_{ambient} is the ambient temperature. Dirichlet-type temperature boundary condition have also been implemented, as well as combinations of convection and Dirichlet for each of the surfaces of the metal can.

2.3 Coupling between electrical and thermal model

The electrical and thermal models are coupled bi-directionally. Within each electrical element, heat is generated through power dissipation in the electrical resistances, both in the electrode pair and in the current collectors. This heat generation is assumed irreversible and contributes to the heat source q in Eq. (3). For the electrodes, the entropy term containing $\frac{\mathrm{d}E_{\mathrm{s}}}{\mathrm{d}T}$, is considered to be reversible and also contributes to the heat source q in Eq. (3). Therefore, the overall heat source q^{El} for the electrode pair is the sum of reversible and irreversible heat [37] as:

$$q^{\mathrm{El}} = \left(\sum_{i=1}^{3} I_i^2 R_i + I^2 R_0 + IT \frac{\mathrm{d}E_{\mathrm{s}}}{\mathrm{d}T} \right) / V^{\mathrm{El}}, \tag{5}$$

where V^{El} is the electrode pair volume in each element. The heat source q^{CC} for current collector is written as:

$$q^{\mathrm{CC}} = \left(\frac{1}{2} \sum_{i=1}^{4} \left(I_i^{\mathrm{CC}} \right)^2 R_i^{\mathrm{CC}} \right) / V^{\mathrm{CC}}, \tag{6}$$

where I_i^{CC} and R_i^{CC} are the current and resistance in the aluminum or copper foil domains, as shown in **Fig. 1**, while V^{CC} is the current collector volume. At each time-step, the heat source from the electrical model is fed as an input into the thermal model,

and the temperature within each thermal element is numerically calculated. The temperature is fed back into the electrical model to update the values of the resistances, capacitances and OCV therein.

In the simulation studies, a distributed model of 1275 electrical/thermal ECN elements was used. Mesh independence of the model results was checked, as discussed in Supplementary Material A. The user-defined meshing was conducted inside the Python model and remained fixed throughout the simulation. The elements are distributed as following (see **Fig. 1**): 5 elements along the angular direction (*x* axis), 15 elements along the axial direction (*y* axis) and 17 elements along the radial direction (*z* axis).

3 Experimental

Experiments were performed on LG M50T (LG INR21700-M50T) cylindrical lithium-ion batteries. These cells utilise a SiO_x-doped graphite negative electrode alongside a $LiNi_{0.8}Mn_{0.1}Co_{0.1}O_2$ (NMC 811) positive electrode, with a nominal capacity of 18.2 Wh (5 Ah). The cell manufacturer's specification sheet lists the upper and lower cut-off voltages as 4.2 V and 2.5 V, respectively. Cells were stored at 10 °C when not in use. All electrochemical experiments were repeated on 3 separate cells simultaneously under the same conditions, to verify repeatability.

All electrochemical data was recorded using a 'Biologic' BCS-815 battery cycler with the accompanying BT-Lab software. The cells being tested for parameterization were housed inside a 'Binder' thermal chamber (KB 23 cooling incubator), set to maintain stable air temperatures between 15 °C and 55 °C, depending on the experiment.

The fan speed of the thermal chamber was set to 100%, placing the cell in a forced air convection cooling regime.

For temperature measurement, K-type thermocouples (TCs) were used throughout the study. The absolute accuracy of all the K-type thermocouple is ±2 ºC. Thermal chamber temperature data was monitored by the built-in thermocouple readers of the BCS-815 battery cycler, logging both temperature and electrochemical data. Cell temperature data was recorded using a Pico TC-08 data logger at a frequency of 1 Hz. Three TCs were attached to the surface of the cell using thermally conductive epoxy resin. The temperature at the centre of the jellyroll was measured using the internal TC using the instrumented cell.

3.1 Parameterization of the electrical network

Experimental data for model parameterization/validation in this study was limited to discharge only. Prior to any discharge experiment, the cells were first charged to 100% SoC using the standard charging procedure outlined in the cell specification sheet. This consisted of a constant current (CC) charge at a C-rate (current divided by nominal capacity) of 0.3 C (1.5 A) until the upper voltage limit of 4.2 V was reached, with a subsequent constant voltage (CV) charge at 4.2 V until the current dropped below 0.01 C (50 mA). This standard charge was always performed at a temperature of 25 °C. The cell was then rested for 2 hours at 25 ºC under open circuit conditions to allow the OCV to equilibrate. We used this starting point to define 100% SoC for subsequent discharge experiments, ensuring a consistent starting point between tests. After per-

forming this standard charge at 25 °C, the temperature of the thermal chamber was adjusted to the set-point required for the subsequent discharge experiment, and the cell held under open circuit conditions until thermal equilibrium under the new ambient temperature was reached.

The numerical values of the circuit components of the electrical model are formulated as lookup tables, whose experimental parameterization is described in this section. Pulse discharge tests were conducted for identifying the values of the electrical circuit components. From pseudo-OCV data for this cell recorded at a current of 0.01 C, a voltage vs SoC curve was produced. This data was then used to tailor a Galvanostatic Intermittent Titration Technique (GITT) experiment for this specific cell, where areas of rapid change in voltage with respect to SoC were identified and used for targeted investigation. Varying the charge passed in each current pulse enabled a high density of data points (every 1% SoC change) in areas of interest in the voltage vs SoC curve, and a lower density of points (4-6% SoC change) where a relatively linear relationship was observed. This approach optimized the resolution of data points across the SoC range, whilst minimizing the test duration. The current during discharge pulses was 1 C (5 A), with a lower voltage cut-off of 2.5 V. Due to slower relaxation of the cell at lower SoC values, the rest periods between current pulses were also extended for the lower SoC regions. This pulsed-current experiment was performed at 5 different temperatures (15 °C, 25 °C, 35 °C, 45 °C, and 55 °C).

The detailed parameter identification procedure and mathematical equations are given in Supplementary Material B. The novel feature of the proposed parameter identification algorithm is that all the model parameters for the full SoC operating range and the 5 temperature levels are simultaneously identified, and constraints imposed on parameter values are used to ensure their smooth transitions across the full temperature range, *i.e.*, the resistance value increases smoothly as the temperature drops. The Root Mean Square Error (RMSE) of the parameterization is 11.7 mV over the whole GITT parametrization process.

3.2 Parameterization of the thermal network

To spatially resolve the computational domain into a set of distributed ECNs for the thermal network, the thickness of each of the cell components is needed. These have been measured for an identical cell using a Scanning Electron Microscope (SEM) [49]. The positive tab is located approximately one third of the distance away from the center along the radial direction, at the top of the jellyroll. The negative tab is situated near the outermost loop, at the bottom of the jellyroll. The tab dimensions were measured to be 165 μm (thickness) × 3.5 mm (width) × 11 mm (length).

Since the entropic term $\frac{\mathrm{d}E_s}{\mathrm{d}T}$ is dependent on cell chemistry and not on its geometry, it is assumed that values from literature experimentally obtained for a pouch cell of similar chemistry (NMC) can be used [27]. In the same vein, the thermal properties of the cell components at material level were also adopted from literature, as are summarized in **Table I**.

Table I. Thickness and thermal properties of cell components [27][50].

Component	Thickness (μm)	Thermal conductivity ($W \cdot m^{-1} \cdot K^{-1}$)	Heat capacity ($J \cdot kg^{-1} \cdot K^{-1}$)	Density ($kg \cdot m^{-3}$)
Aluminum foil	16.33	238.00	903.00	2702.00
Copper foil	27.00	398.00	385.00	8933.00
Anode	86.15	1.58	1437.00	1555.00
Cathode	77.03	1.04	1270.00	2895.00
Separator	14.00	0.34	1978.00	1017.00
Can	160.00	238.00	903.00	2702.00

3.3 In-cell thermal sensor application

To enable internal thermal monitoring of the cells, necessary for the validation of the proposed model, K-type thermocouples were inserted in the cell core. The measurements were taken at the central cell axis, mid-height of the jellyroll, with complementary sensors attached to the cell surface during testing. Before modification, cell disassembly was conducted to check the geometrical facts of LG M50T. The positive and negative sides are as shown in **Fig. 2**(a) and (b), respectively.

For modification, fresh cells were discharged to their minimum operating voltage of 2.5 V as specified by the manufacturer, and transferred to a positive-pressure Argon glove box with O_2 and H_2O traces below 0.1 ppm. This ensures no atmospheric contamination enters the cells during modification. The cells were opened along the edge of the positive terminal cap and the thermal probe was inserted as shown in **Fig. 2**(c). This procedure uses the core of the jellyroll, left free of layers in the manufacturing process, after the mandrel winding the jellyroll is removed. The probe tip rests against the surplus layer of the separator material, from the inside loop of the jellyroll. Finally, the cathode cap was re-sealed using a narrow strip of fast-setting resin. Impact of the modification on the cells performance has been thoroughly evaluated previously [51], and found negligible, including no noticeable electrolyte loss. The approach utilised

here is a highly transferrable methodology for experimental characterisation of the cell's internal thermodynamics, which is described in detail in prior publications [51,52].

The electrochemical performance of the instrumented cell was compared to that of an unaltered cell. The 0.3 C constant current discharge experiments and pulsed-current discharge experiments described previously for model parameterization were performed on three instrumented cells and one fresh cell, to quantify differences introduced by instrumentation in their capacity and resistance. All experiments were performed in a thermal chamber at 25 °C. These tests revealed no significant differences between the instrumented and unaltered cells (see **Fig. 2**(d) and (e)). The instrumented cells were therefore deemed suitable for use in model validation experiments.

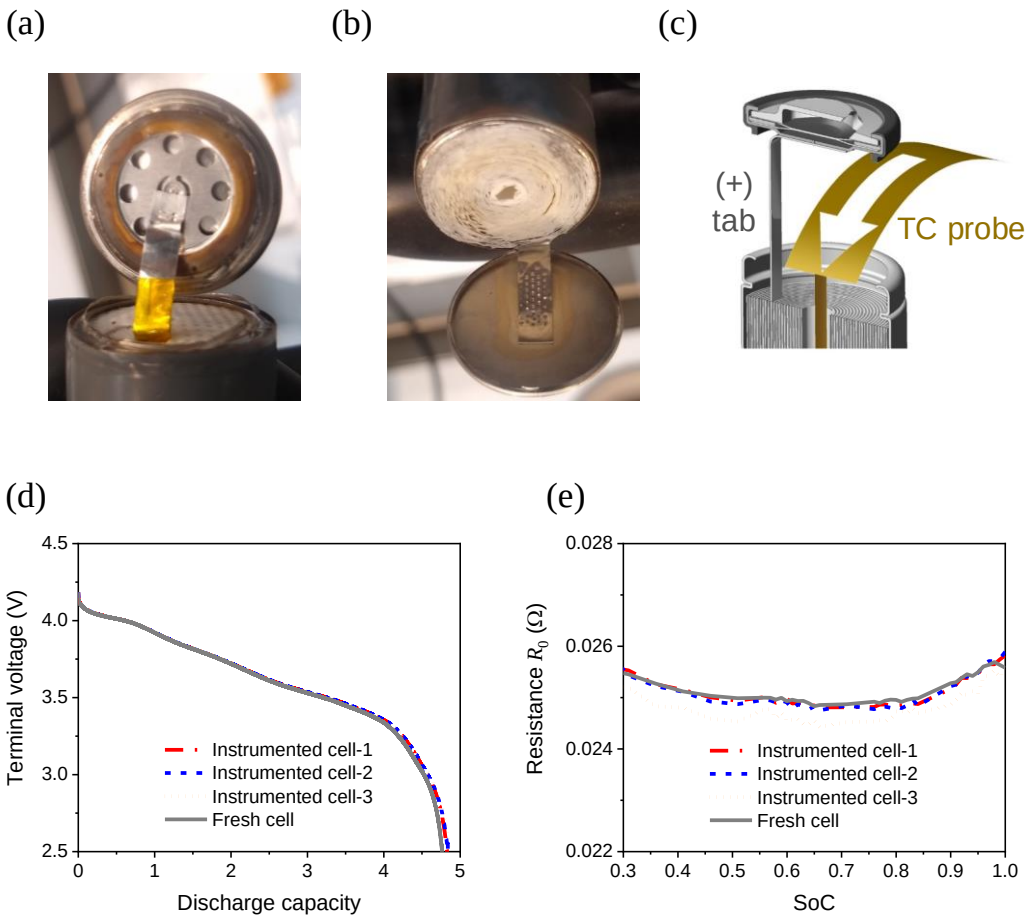


Fig. 2. Illustration of a cylindrical cell instrumentation with a thermal probe. (a) Positive and (b) negative side of LG M50T. (c) The concept of the sensor insertion process. (d) Terminal voltage during the 0.3 C constant current discharge and (e) resistance R_0 in the pulsed current discharge experiments for three instrumented cells and an unaltered one.

4 Results and Discussion

4.1 Model validation

4.1.1 Thermal model validation

Thermal validation of the model was performed by testing the thermal response of the cell under no electrical load. In these experiments, instrumented cells were sub-

jected to rapid temperature changes between two set values, with reading from the internal TC being used for verifying the transient temperature response. Cells were submerged in a vat of thermally conductive, electrically insulating base oil (Etro 4+), freely suspended using the thermocouple wires as supports. The vat of oil was held at a constant temperature, T_1. Once the cell had thermally equilibrated at this first set point, it was then rapidly transferred to a second vat of oil which was held at a second set temperature, T_2, and again allowed to come to thermal equilibrium. The temperatures on the surface and center of the cell were recorded throughout. This experiment was repeated with both a positive (25 °C to 45 °C) and negative (45 °C to 35 °C) temperature change, and using multiple cells in each direction (5 repeats in total).

In the simulation setup, the surface temperature of the cell is chosen as the Dirichlet boundary condition for each of the two experiments. **Fig. 3**(a) shows the thermal model validation for the positive temperature change. The green curve shows the step increase in surface temperature from 25 °C to 45 °C upon immersion in the vat. It is seen that the simulated core temperature, denoted by the red dashed curve, closely tracks the experimentally measured values from the internal TC (denoted by the solid black line). **Fig. 3**(b) shows the corresponding response for the negative temperature change from 45 °C to 35 °C. As seen from **Fig. 3**(a) and (b), the simulation results show good agreement with the experimental results with RMSE of 0.21 °C and 0.25 °C, respectively. These results provide a validation of the thermal model under no current load conditions.

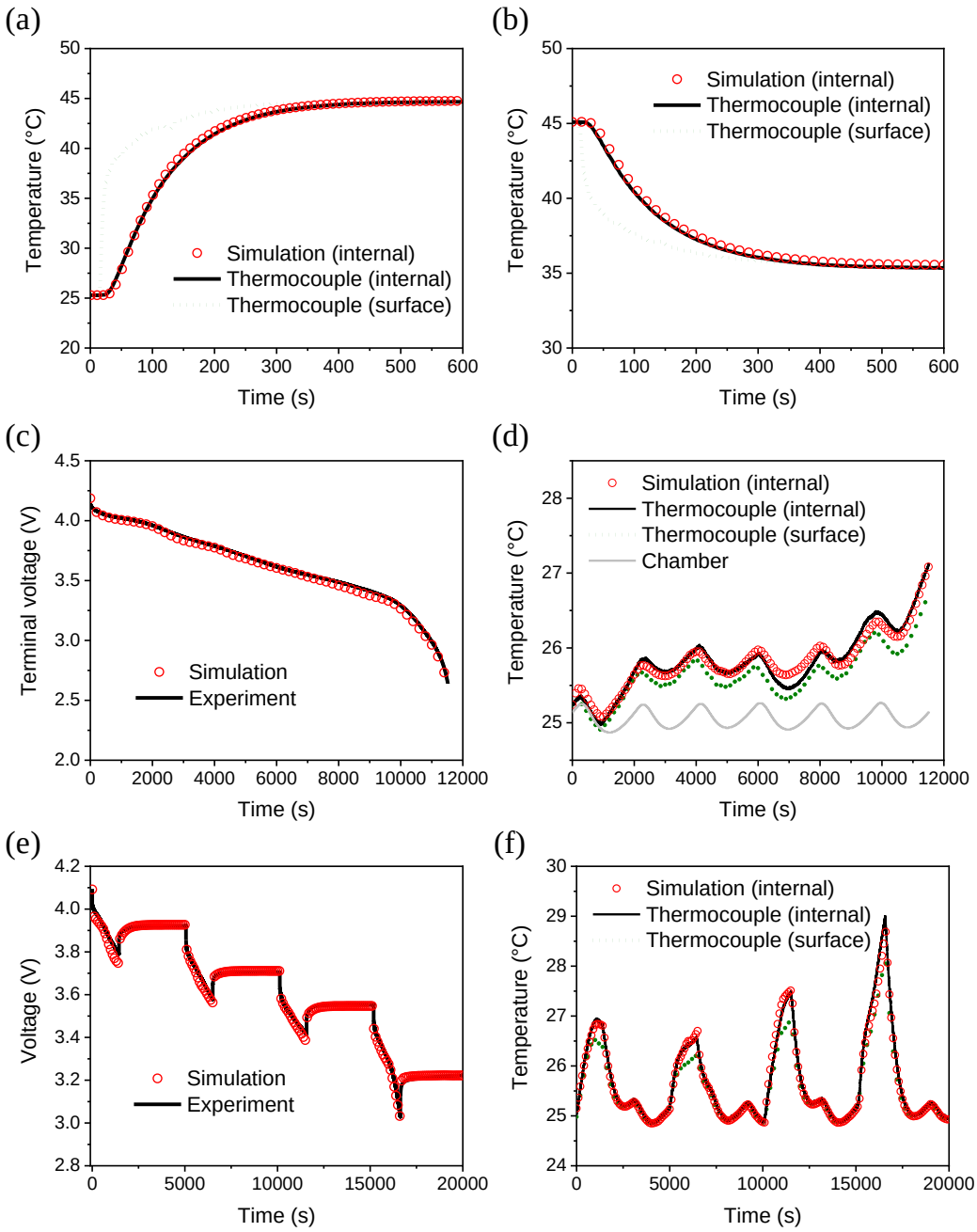


Fig. 3. Model validation: simulation and experimental results for (a) temperature change from 25 °C to 45 °C and (b) temperature change from 35 °C to 25 °C. Coupled electrical-thermal model validation: terminal voltage (c) and temperature (d) during an 0.3 C constant current discharge; and terminal voltage (e) and temperature (f) during a 0.5 C pulse discharge, in which a step discharge current at 0.5 C is followed by 1 h of relaxation. The experimental tests were repeated twice for (a) and three times for (b-f). The repeated results are highly reproducible with RMSE of 0.15 ºC, 0.20 ºC, 1.75 mV, 0.25 ºC, 6.74 mV and 0.35 ºC for (a-f), respectively. For simplicity, only the first test

result is shown in (a-f).

4.1.2 Coupled model validation under thermal management

For coupled thermal and electrochemical validation of the model, two types of discharge test were performed: a CC discharge at 0.3 C (1.5 A), and a pulsed-current discharge at 0.5 C (2.5 A). In the pulsed-current experiment, each pulse equates to a 20% SoC change, with 1 hour rest periods between pulses. As can be seen from the temperature data in **Fig. 3**(d), there is a periodic oscillation in the air temperature inside the chamber due to the proportional-integral-derivative (PID) control (with an amplitude of approx. ±0.25 °C). This fluctuating cell surface temperature was used as the temperature boundary condition for the metal can in the model.

As shown in **Fig. 3**(c), for a constant current discharge of 0.3 C, the simulated terminal voltage matches the experimental results with an RMSE of 23.31 mV. For the pulsed discharge test, the terminal voltage during the 4 pulses are shown in **Fig. 3**(e). The simulated terminal voltage shows good agreement to experimentally measured cell voltage with an RMSE of 15.38 mV. Similarly, the RMSE of the cell's core temperature is 0.09 °C and 0.10 °C for the constant current and pulse discharge tests respectively. The good agreement between simulated results and experimental data provides confidence in the model's fidelity in this regime of operation.

4.2 Electro-thermal inhomogeneity within the cell

During normal discharge and charge operation, electro-thermal inhomogeneities

exist within the cell, which strongly influences its performance. Previous research has shown that cells with large thermal gradients, and hence with large electro-thermal inhomogeneities, shall experience an significantly accelerated loss of capacity [10]. Owing to this, monitoring and controlling the cell's electro-thermal performance becomes difficult as its internal states cannot be measured by sensors mounted on the surface. In this section, the effect of electro-thermal inhomogeneity is quantified, by simulating the states of the 5 Ah cylindrical cell under convective boundary conditions on all surfaces (convective heat transfer coefficient is 50 W/(m^{2}K) under 25 °C) during a 1 C discharge. Initially, all the physical fields are uniform within the cell domain. **Fig. 4**(a-d) show snapshots for the internal quantities after 1000 seconds of discharge. Distinct, non-uniform internal gradients for the temperature, current density, SoC and OCV are visible. These inhomogeneities can be explained as follows: under the convective cooling boundary condition, the thermal gradient exist in the radial direction, as shown in **Fig. 4**(a), *i.e.* temperature in the core is higher than that near the outer surface. The current density therefore becomes inhomogeneous due to the reduced local electrical resistance under higher temperature, as shown in **Fig. 4**(b). As time evolves, the core is discharged faster so that SoC for the core is lower than that of the outer regions (see **Fig. 4**(c)), and thus a similar gradient forms for the OCV (see **Fig. 4**(d)).

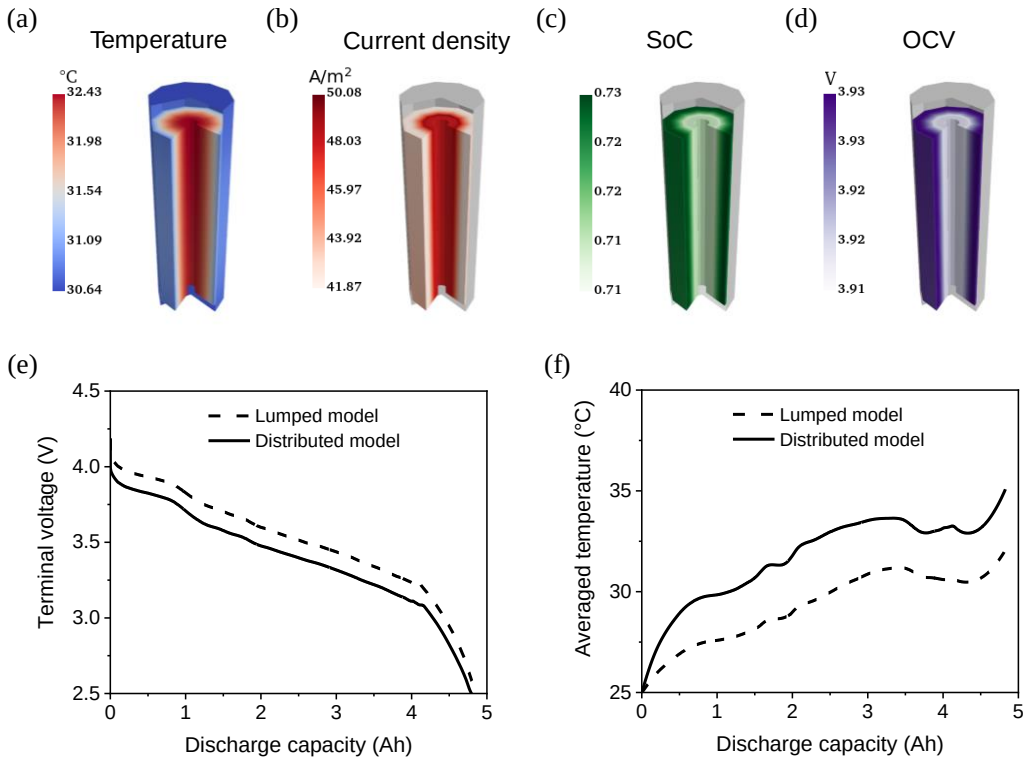


Fig. 4. For a 1 C discharge under convective boundary conditions, a snapshot of simulation results after 1000 s of discharge for (a) temperature, (b) current density, (c) SoC and (d) OCV. For the same discharge process, (e) a comparison of terminal voltage output between lumped and distributed model, and (f) a comparison of average cell temperature between lumped and distributed model.

The performance of the distributed electrical and thermal model was compared with that of the lumped (or standard) cell model, for the same initial and boundary conditions. In the lumped model, there is only one electrical ECN and one thermal ECN for the entire cell. The same equations Eq. (1-5) can be applied computationally either as a lumped model or as a distributed model. The terminal voltage output (**Fig. 4**(e)) and the average cell temperature (**Fig. 4**(f)) vary significantly between the two models. The voltage output for the lumped model is consistently and significantly higher than

that of the distributed model, by up to 100 mV. The simulated average internal temperature of the cell increases during the discharge by around 30% less in the lumped model compared to the distributed model. These differences highlight that tot only are lumped models a poor approximation of cell behavior, they are also a dangerous one, potentially leading to overestimation of the available energy and instantaneous power, and to underestimation of the cell temperature for cell and pack design, estimation and prediction.

4.3 Influence of cooling strategy

A series of parametric studies are performed using the distributed thermal-electrical coupled model in order to understand the effect of cooling choice on cell performance.

In the majority of cylindrical cell model studies [11,25,33,53,54], the boundary conditions are applied directly on the jellyroll surface. However, in a real cell, the jellyroll is enclosed inside a metal can and therefore, the boundary conditions should, in principle, be applied on the can. There are many features of the internal cell design, such as a gap between the jellyroll and the top of the can, that affect heat generation and transport between jellyroll and can, which thus necessitate simulating in an entire cell assembly. For comparison purposes, the effect of cooling choice is studied on the two scenarios: model of the *jellyroll only*, and the more realistic model of the *jellyroll and can*.

Two sets of common cooling schemes *viz.* top/base cooling and side cooling are used. For top/base cooling, only the top and base surfaces are cooled, while the side surface is thermally insulated, similar to base-plate cooling in automotive packs. For

side cooling, only the side curved surface is cooled, while the top/base surfaces are thermally insulated, similar to ribbon cooling in automotive packs. In each of these cases, both conduction and convection modes of cooling are simulated. To exclude the influence of tab design, all simulations employ a single-tab (variant-b) configuration, as found in the LG M50T cells.

For the *jellyroll only* model, the average cell temperature and its standard deviation (SD), used as a descriptor of temperature inhomogeneity within the cell, are shown in **Fig. 5**(c, e). The thermal gradient forms mostly along the radial direction for the side conduction cooling, and mostly along the axial direction for the top/base conduction cooling, as seen in **Fig. 5**(a). Among the four cooling schemes employed, the top/base conduction cooling is the most effective: during the whole discharge process, the cell average temperature is maintained close to the external sink temperature (**Fig. 5**(c)) and exhibits the smallest temperature SD (**Fig. 5**(e)). This is attributed to the following two reasons. Firstly, the heat transfer rate by conduction is much higher than convection, *i.e.* more heat is extracted by conduction than convection given the same temperature difference and cooling area. Secondly, the area being cooled in top/base cooling has direct contact to the current collector foils. These foils have high thermal conductivities (as seen in **Table I**) and provide fast thermal pathways for dissipating the heat generated within the jellyroll.

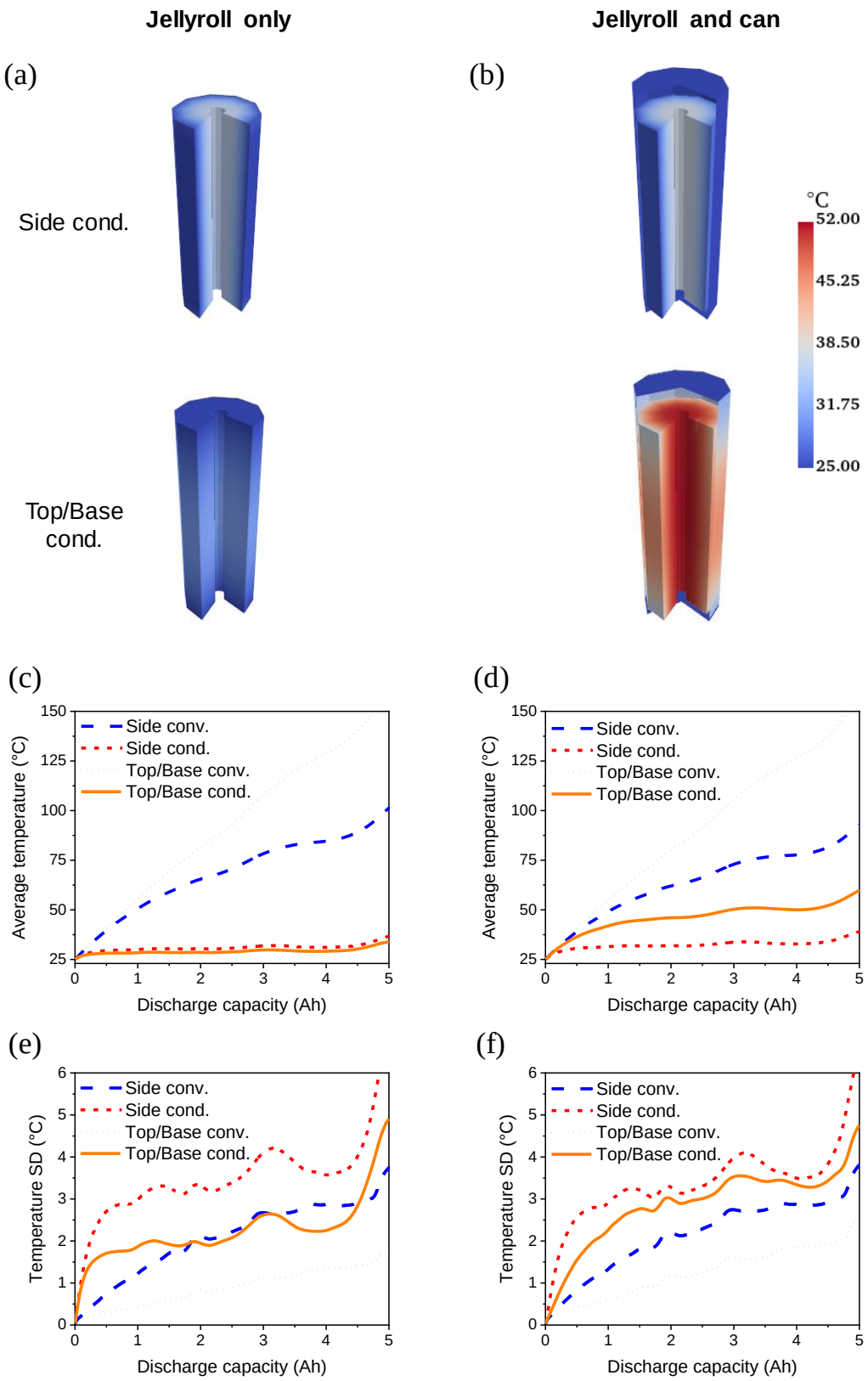


Fig. 5. Cell thermal predictions from the *jellyroll only* model (left column) and the *jellyroll and can* (right column) under different cooling schemes during a continuous 3 C discharge. (a-b) Internal temperature distribution at the end of discharge. (c-d) Variation

of average temperature with discharge capacity. (e-f) Variation of standard deviation with discharge capacity. Convection and conduction are abbreviated as conv. and cond., respectively. The convective heat transfer coefficient is 50 W/(m^{2}K); both forced air convection and the conduction boundary condition are set to 25 °C.

As seen from **Fig. 5**(c) and (e), employing the side conduction in the *jellyroll only* arrangement leads to a higher temperature rise as well as a larger temperature distribution relative to the top/base conduction. The cooling area for side conduction is larger than that of the top/base conduction, which facilitates heat extraction. However, as shown in Eq. (7) and Eq. (8), the internal thermal conductivity in the radial direction (*z* direction in the model schematic **Fig. 1**) is significantly smaller than that in the axial direction (*y* direction in the model schematic **Fig. 1**). The equivalent (lumped) thermal conductivity in the axial direction can be calculated as:

$$\lambda_y^{\mathrm{eq}} = \frac{\lambda^{\mathrm{Cu}}\delta^{\mathrm{Cu}} + \lambda_y^{\mathrm{El}}\delta^{\mathrm{El}} + \lambda^{\mathrm{Al}}\delta^{\mathrm{Al}} + \lambda_y^{\mathrm{El}}\delta^{\mathrm{El}}}{\delta^{\mathrm{Cu}} + \delta^{\mathrm{El}} + \delta^{\mathrm{Al}} + \delta^{\mathrm{El}}} = 37.91\,(\mathrm{W\cdot m^{-1}K^{-1}}), \tag{7}$$

while the equivalent thermal conductivity in the radial direction is given by:

$$\lambda_z^{\mathrm{eq}} = \frac{\delta^{\mathrm{Cu}} + \delta^{\mathrm{El}} + \delta^{\mathrm{Al}} + \delta^{\mathrm{El}}}{\delta^{\mathrm{Cu}}/\lambda^{\mathrm{Cu}} + \delta^{\mathrm{El}}/\lambda_z^{\mathrm{El}} + \delta^{\mathrm{Al}}/\lambda^{\mathrm{Al}} + \delta^{\mathrm{El}}/\lambda_z^{\mathrm{El}}} = 1.17\,(\mathrm{W\cdot m^{-1}K^{-1}}), \tag{8}$$

where $\delta^{\mathrm{Cu}}, \delta^{\mathrm{Al}}, \delta^{\mathrm{El}}$ are the thicknesses of copper foil, aluminum foil and electrode pair (including separator), while λ^{Cu}, λ^{Al} are the isotropic thermal conductivities of copper and aluminum foils, and λ_y^{El}, λ_z^{El} are the electrode pair thermal conductivities in the axial and radial direction. Therefore, for the side conduction cooling scheme, the thermal performance is limited by the relatively low internal heat transfer conductivity in the radial direction. The *true* radial direction thermal conductivity may in fact be considerably lower than the ideal value calculated here, as was found in experimental

studies on cylindrical cells [55–57], due to additional interfacial thermal resistances. Considering the number of electrode pair layers in a cylindrical cell, the interfacial thermal resistance can become significant, thus further limiting heat transfer in radial direction. As the model predictions are in good agreement with the validation experiments, further improvements to the thermal characterization of the cell are left for further work.

As shown in **Fig. 5**(a, b), the thermal predictions of the *jellyroll and can* model are radically different to that of the *jellyroll only*. **Fig. 5**(d) shows the conduction schemes are better than the corresponding convection counterparts in terms of maintaining a lower average temperature. The average temperature rise for side conduction is this time significantly lower than that for top/base conduction due to the larger cooling area, unlike in the case where the presence of the can and associated thermal paths were ignored.

While the top/base convection cooling leads to the smallest temperature SD (**Fig. 5**(f)), this is merely due to the fact that the cell is close to experiencing adiabatic boundary condition, making this cooling strategy a poor choice.

Based on the predictions of the *jellyroll and can* model, it can be concluded that side conduction cooling is the most effective way to cool these cells, striking a balance between keeping the average cell temperature relatively low, while not creating significant temperature gradients within the cell. Critically, this is a different cooling choice than that recommended based on the more idealized *jellyroll only* model, demonstrating the importance of using models with can when studying the effect of cooling choices on battery systems performance.

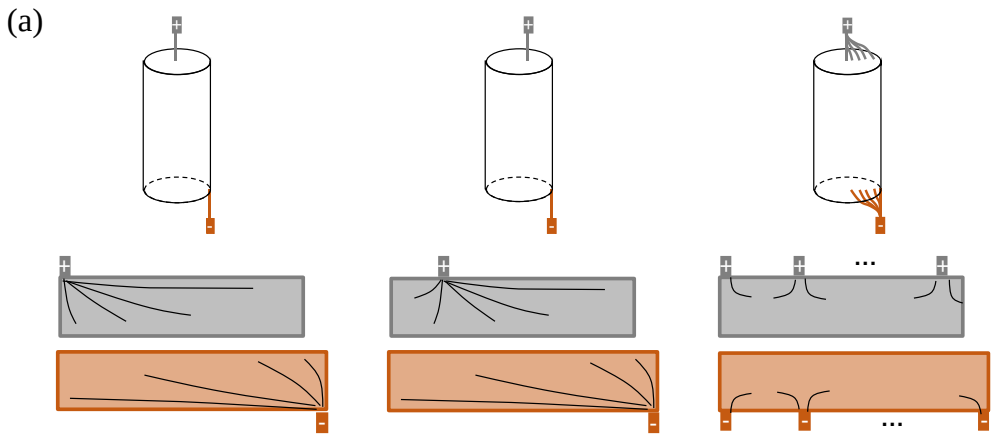
4.4 Influence of tab design on thermal behavior

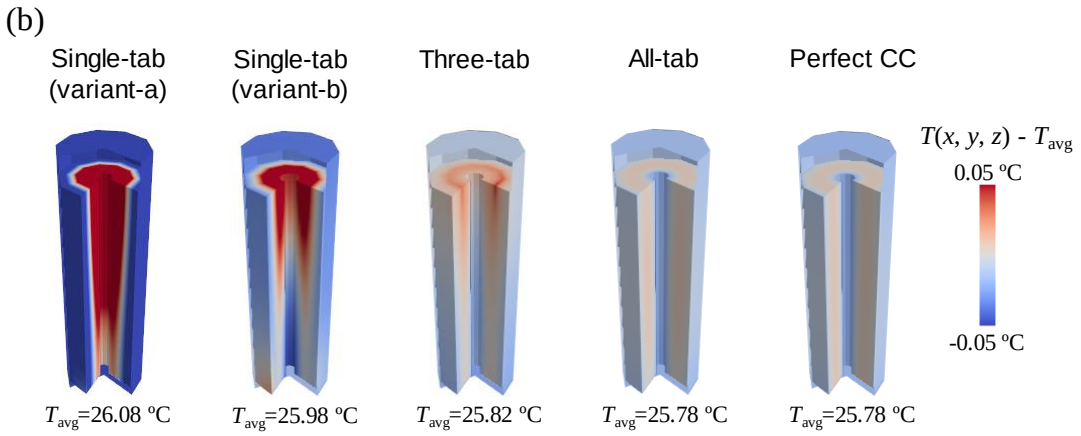
In addition to the cooling strategy, tab design also plays an important role in the performance of cylindrical cells [17,58,59]. In this section, the effect of the number of cell tabs and their geometric placement is studied through simulation. For simplicity, the cooling approach is fixed at adiabatic thermal boundary conditions and effect of entropy is excluded. Single-tab design is common in cylindrical cells: one tab for the positive and one for the negative current collector. The current density can be significantly higher near the tabs, as schematically illustrated in **Fig. 6**(a), and significantly larger heat generation can occur in the regions near tabs. This current inhomogeneity can be reduced by increasing the number of cell tabs, as schematically shown in **Fig. 6**(c). Even moving the tab to a location different from the end of the current collector can reduce the maximum current density and resulting heat generation inhomogeneity, as schematically shown in **Fig. 6**(b).

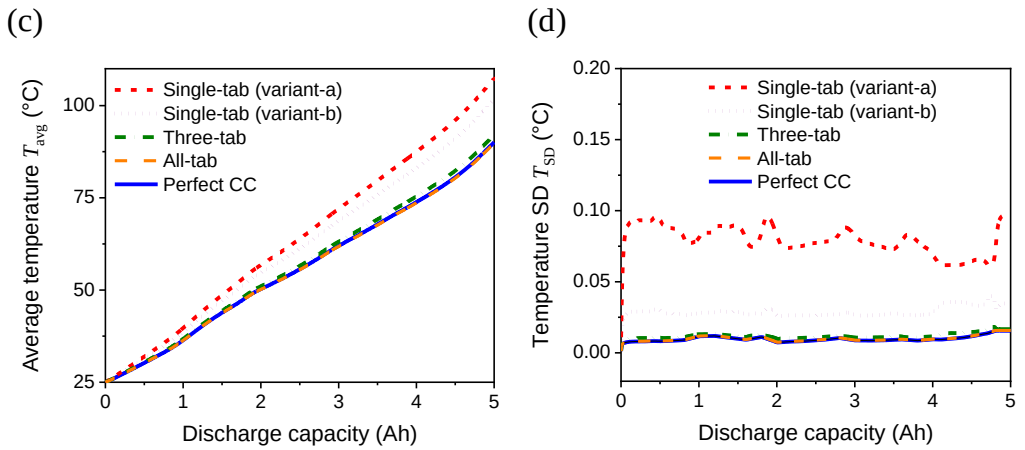
The following tab designs are considered in the study, in order of increasing complexity:

- Single-tab (variant-a) describes the scenario of one negative tab located at the outermost end of the copper foil, and one positive tab located at the innermost end of the aluminum foil.
- Single-tab (variant-b) describes the scenario of one negative tab located at the outermost end of the copper foil, and one positive tab located at a third of the position, away from the jellyroll innermost end; this configuration represents the structure of the LG M50T cell.

- Three-tab describes the scenario of three cell tabs placed at evenly spaced intervals along the jellyroll radial direction, for positive and negative side.
- All-tab describes the scenario of all 22 cell tabs placed at evenly spaced intervals along the jellyroll radial direction, for positive and negative side, mimicking the configuration of the ‘tabless battery’ [28].
- Perfect CC describes the scenario of ideal current collectors with zero electrical resistance and thus zero heat generation in the current collectors, which is used for reference.


(a)


(b)
Single-tab (variant-a)
Single-tab (variant-b)
Three-tab
All-tab
Perfect CC
T(x, y, z) - T_avg
0.05 ºC
-0.05 ºC
T_avg=26.08 ºC
T_avg=25.98 ºC
T_avg=25.82 ºC
T_avg=25.78 ºC
T_avg=25.78 ºC


(c)
Average temperature T_avg (°C)
Discharge capacity (Ah)
Single-tab (variant-a)
Single-tab (variant-b)
Three-tab
All-tab
Perfect CC
(d)
Temperature SD T_SD (°C)
Discharge capacity (Ah)

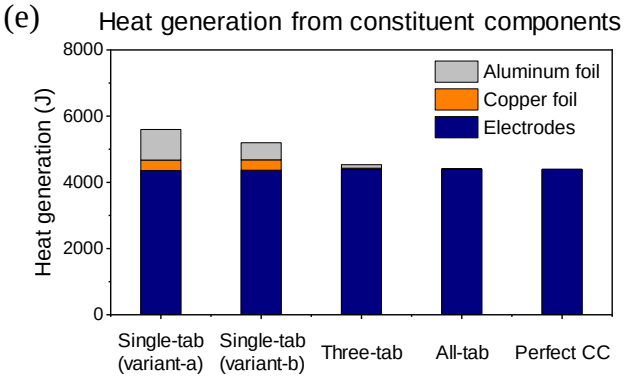

(e)
Heat generation from constituent components
Heat generation (J)
Aluminum foil
Copper foil
Electrodes
Single-tab (variant-a)
Single-tab (variant-b)
Three-tab
All-tab
Perfect CC

Fig. 6. Model predictions of the influence of cell tab design on cell performance. (a) Schematic of jellyroll in wound and unwound view for three-tab configurations: single-tab (variant-a), single-tab (variant-b) and multi-tab. Flux lines in the unwound view denote current density magnitude, schematically describing higher current densities in the tab regions. (b) Inner temperature values for five different tab designs after the first 60 s of discharge at 1 C. Throughout the discharge: Evolution of the average temperature (c), temperature standard deviation (d) and total heat generation from the aluminum foil, copper foil and electrodes (e) for the five tab designs.

Fig. 6(b), the temperature contours near the very start of a discharge (60 s of discharge), shows that significant temperature gradients are created within a short time solely due to the number and position of the tabs, even before the positive feedback between current and temperature occurs. Configurations with more tabs reduce this effect and lead to both smaller temperature variation and smaller rise in average temperature. For the cell with single-tab configuration (variant-a), the average temperature reaches 107.33 °C at the end of discharge (**Fig. 6**(c)). The three-tabs and all-tab configurations exhibit lower maxima for the average temperature at the end of discharge, 92.02 °C and 89.76 °C respectively. Both values are relatively close to the ideal configuration of perfect CC. The more tabs the better. The single-tab (variant-b) configuration shows that the position of the tab also affects the cell average temperature: moving the tab a third of the distance away from the coil center reduces the temperature rise by 5.17% (**Fig. 6**(c)). This improvement occurs because the positive tab region has the hottest temperature, and single-tab design (variant-b) moves this hottest spot towards outside compared with single-tab design (variant-a) for more effective heat dissipation.

Fig. 6(e) illustrates the model production for the total heat generated by the aluminum foil, copper foil and electrodes during the discharge of cells with different tab designs. In single tab configurations a small but not negligible amount of heat is generated due to the non-ideal current collectors. Compared with the perfect CC configuration, the current collector resistance is effectively higher in cells with fewer tabs due to the longer current pathway between positive and negative tab [25]. For the current collector dimensions and electrical conductivities assumed here, more heat is generated by the aluminum than by the copper current collector, leading to the jellyroll to exhibit higher temperatures at the end of the positive terminal, as shown in **Fig. 6**(b).

Large temperature gradients within the cell have been shown to severely affect cell performance and accelerate degradation [10]. Hence, it is beneficial to optimize tab design to minimize inhomogeneity. The standard deviation of cell internal temperature is compared for the five different tab configurations. It is shown in **Fig. 6**(d) that configurations with more cell tabs reduce both heat generation and temperature inhomogeneity, which is consistent with the claims in the patent by Tesla Inc. for a cell with a continuous tab [28].

In order to identify the mechanisms leading to the observed behavior, the heat generation, temperature and current density across electrodes are analyzed for two of the five tab configurations considered: single-tab (variant-b) and all-tab. The value of the local inner temperature is mirror of the magnitude of the current density, as shown in **Fig. 7**(c, e) for single-tab design and **Fig. 7**(d, f) for all-tab design, both after 60 s into a 1 C discharge. Higher temperatures lead to higher current densities, due to smaller

local resistance. In turn, the larger current density leads to increased local heat generation, thereby further raising the local temperature, resulting in a positive feedback loop. In the single-tab cell, the initial heat generation rate in the tab region of the current collector is significantly higher than in the rest of the current collector **Fig. 7**(a).

Due to the positive feedback between temperature and current, the initial inhomogeneities are further exacerbated as the discharge progresses. As a consequence, the standard deviation for single-tab (variant-a) increases rapidly and remains above all other configurations as previously shown in **Fig. 6**(d). For the all-tab configuration, as shown in **Fig. 7**(b), the heat generation rate is two orders of magnitude lower than the single-tab (variant-b) case, thereby mitigating the positive feedback. Although there exists a slight temperature gradient between core and cell surface, the temperature is mostly uniform throughout the cell.

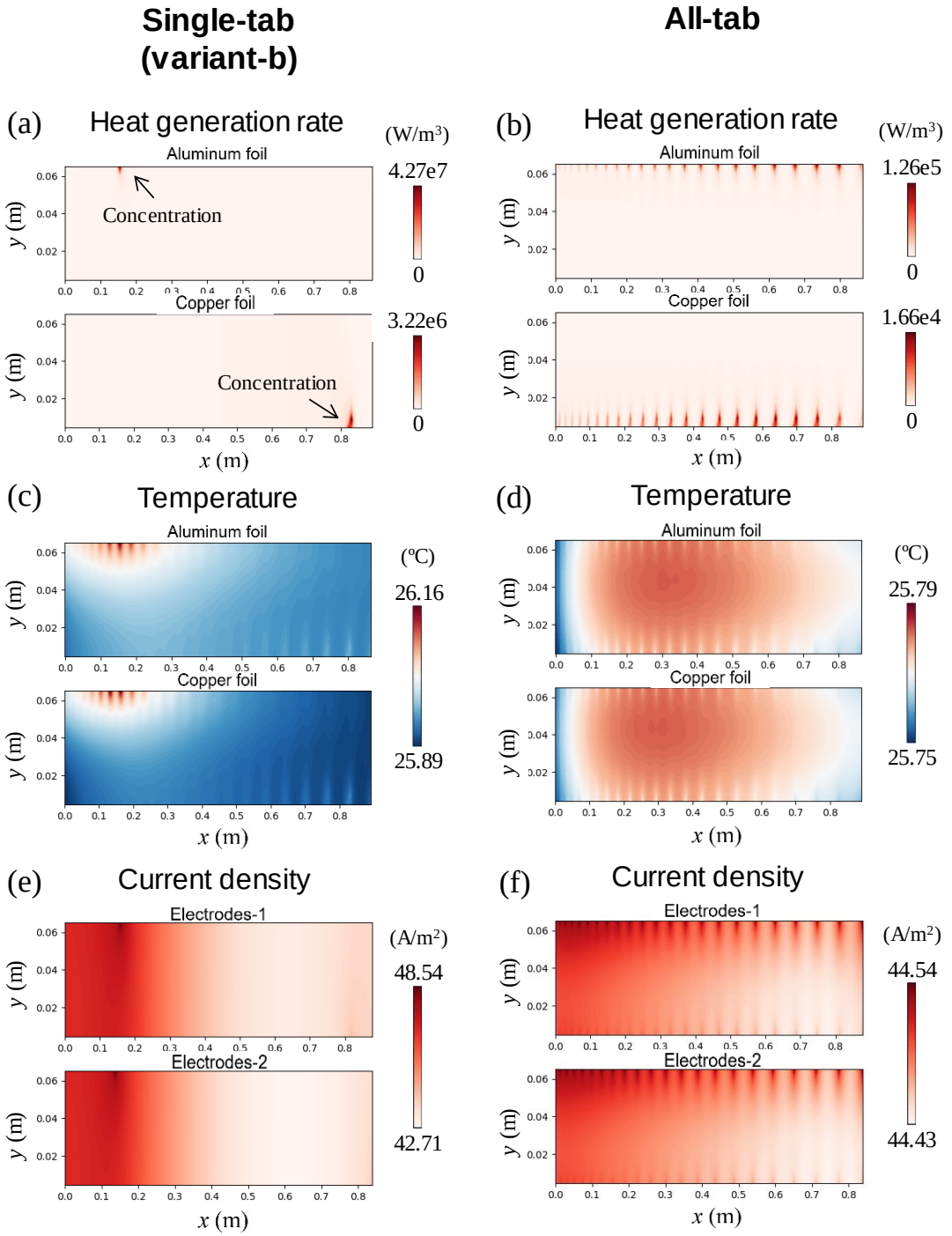


Fig. 7. Comparison of single-tab (variant-b) and all-tab design in unwound view, after 60 s of discharge at 1 C. Heat generation rate of the two current collector foils for (a) single-tab design and (b) all-tab design. The increased heat generation rate near the tabs (a) is due to all current being guided through the tab. The peak heat generation rate in (a) is two orders magnitude higher than (b) as shown by the colorbar scale. Local temperature profile of the two current collector foils for (c) single-tab design and

(d) all-tab design. Current density profile of the two electrode layers for (e) single-tab design and (f) all-tab design. For visibility, the colorbar scales for the two tab designs are not the same.

4.5 A new strategy for cell performance optimization

Choosing the most performant combination of thermal management and tab design is complicated by cost and manufacturing considerations, as well as the fact that studies such as those in **Fig. 5** may not always provide clear-cut recommendations. In this section, two quantitative metrics named 'average function value' are presented for quantitatively evaluating the combined effectiveness of thermal management strategies and cell tab design. The two metrics are related to the two goals of an effective cooling system: to maintain the cell temperature close to a given target and to minimize temperature gradients within a cell. **Fig. 8**(a-b) schematically shows the evolution of the average internal temperature $T_{\text{avg}}(t)$ and the internal temperature standard deviation $T_{\text{SD}}(t)$ during a continuous current discharge, under a given thermal management scheme. Importantly, this study can be made for any other usage type representative for a given application, including for a drive cycle.

The first metric introduced here measures the ability of the cooling approach to maintain the cell internal average temperature close to a target value: ΔT_{avg} represents the difference between the instantaneous average internal cell temperature $T_{\text{avg}}(t)$ and the temperature targeted by the cooling choice T_{target}, time-averaged over the discharge process:

$$\Delta T_{\text{avg}} = \frac{S_1}{t} = \frac{1}{t}\int_0^t (T_{\text{avg}}(t) - T_{\text{target}}) \cdot \mathrm{d}t \,. \tag{9}$$

Here S_1 is the integral of the temperature difference over time t, and T_{target} is set here to 25 ºC. Under more efficient cooling schemes, $T_{\text{avg}}(t)$ is expected to converge to the targeted temperature sooner and result in a lower ΔT_{avg} over the run.

The second metric introduced here measures the ability of the cooling approach to maintain temperature gradients within a cell to a minimum: ΔT_{SD} represents the temperature inhomogeneity time-averaged over the discharge process, expressed as:

$$\Delta T_{\text{SD}} = \frac{S_2}{t} = \frac{1}{t}\int_0^t T_{\text{SD}}(t)\cdot \mathrm{d}t \,. \tag{10}$$

Here S_2 is integral of the internal temperature standard deviation over time *t*.

For better cell performance, both ΔT_{avg} and ΔT_{SD} should be minimized. Various combinations of different tab designs and cooling schemes are simulated using the distributed thermally coupled ECN model developed in this work, and the predicted ΔT_{avg} and ΔT_{SD} for each case are shown in **Fig. 8**(c) for a 3 C constant current discharge. For clarity, only single-tab (variant-b) and all-tab results are shown here. For cooling schemes, only convection or conduction are applied on the side or base surfaces, forming four cases: (1) side and base convection, (2) side convection and base conduction, (3) side and base insulation and (4) side and top and base conduction. The top surface is thermally insulated in cases (1), (2) and (3) as it usually carries the electrical connections in battery packs. Simulations were also performed for two other cases: (5) side conduction and base conduction and (6) side conduction and base convection. Their results overlap within numerical error to the results from case (4), showing that there is little to be gained from top/base cooling once the side is conductively cooled.

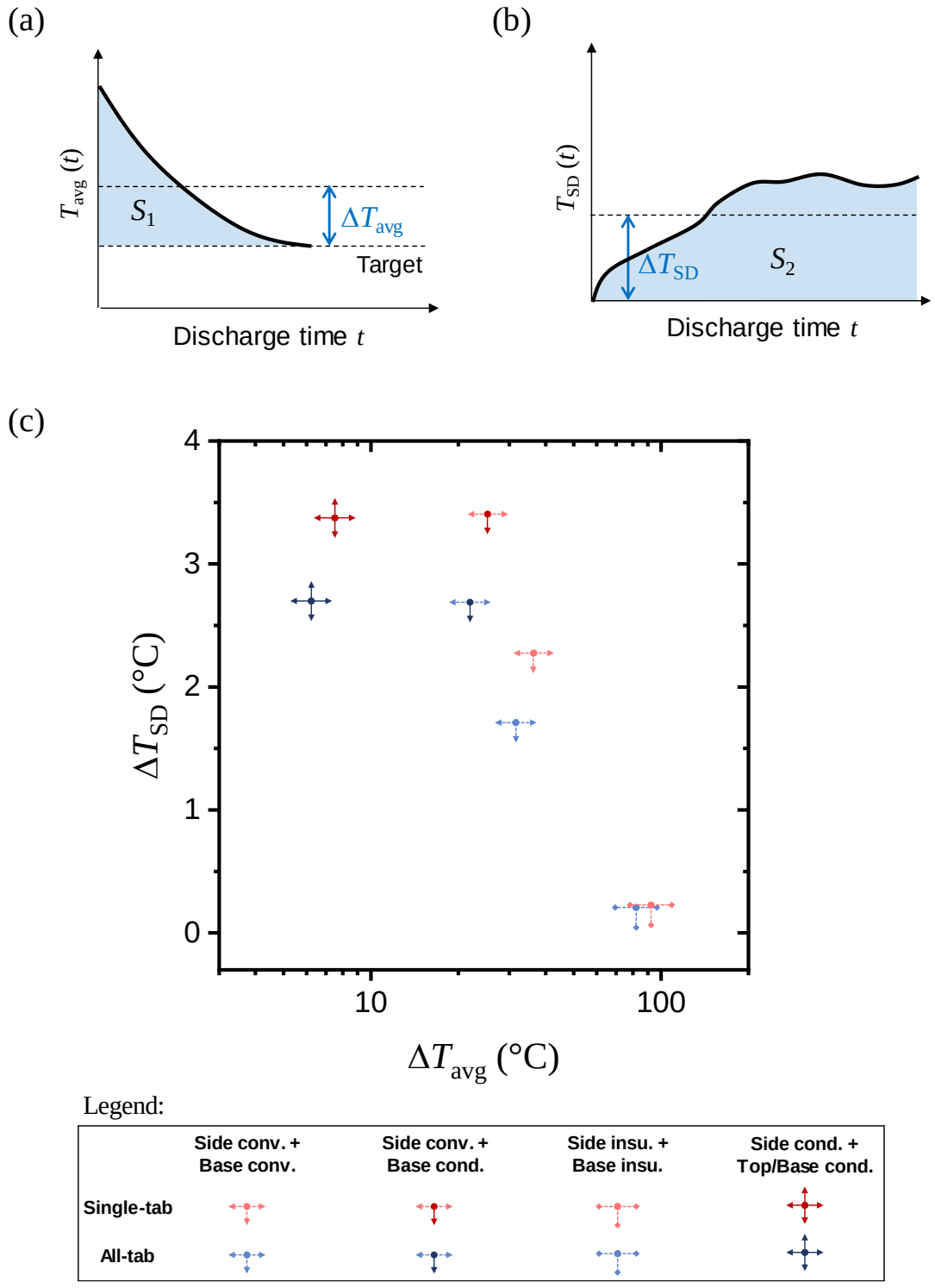


Fig. 8. During a 3 C constant current discharge (a) schematic of the new metric ΔT_{avg}: the time-averaged temperature difference between the instantaneous average internal cell temperature and the targeted cooling temperature, and (b) schematic of the new metric ΔT_{SD} : the time-averaged standard deviation of the internal temperature.

(c) Model-predicted values for the two metrics for cylindrical cells with single-tab (variant-b) design (red) and all-tab design (blue) under cooling schemes. The symbols denote cooling schemes as defined in the legend of (c). Convection, conduction and insulation are abbreviated as conv., cond. and insu., respectively. The convective heat transfer coefficient is 50 W/(m^2K); both forced air convection and the conduction boundary condition are set to 25 °C. Two other cases were simulated, side & base conduction and side conduction & base convection, and were found to give the same results as the case of side & top/base conduction.

The results in **Fig. 8**(c) show that there is generally a trade-off between the ability of a given cooling method to maintain a low cell average temperature and that to minimize thermal gradients within the cell. Insulated cells and convective-only cooled cells exhibit marked increases in temperature over the discharge process, as the horizontal axis in **Fig. 8**(c) is logarithmic.

The cell with the all-tab design is always cooled more effectively and evenly than the one with single-tab design, but the benefits are particularly prominent in the cases of conduction cooling. The two metrics are reduced by 13.55% and 25.41%, respectively under convective cooling. This conclusion justifies the claims in Tesla's patent for a cell with a continuous tab [28].

Side conduction cooling (with base convection cooling) and base conduction cooling (with side convection cooling) are both commonly utilized in battery modules. As mentioned above, predictions from the side conduction base convection case are the same as those for side and base conduction in **Fig. 8**(c). These predictions indicate that, were a battery pack designer to choose one over the other, then conductively cooling the side is more effective at cooling than conductively cooling the base, mostly due to

the larger cooling area at the sides. In the case of single-tab cells, conductively cooling the side also lowers the thermal gradients within the cell.

For pouch cells, where cooling the tabs rather than cell surface has been shown to provide marked benefits for minimizing the thermal gradients even when tab contact area is lower than surface contact area [27]. To the contrary, in the case of cylindrical cells it is the size of the cooling area that determines the better cooling approach, due to the fact that the can provides a path of high thermal conductivity all around, making side cooling an uncontested winner.

5 Conclusions

The first three-dimensional distributed coupled electro-thermal equivalent circuit network (ECN) model is developed for a cylindrical lithium-ion battery. The model accounts for the spiral structure of the jellyroll both in the electrical and thermal domains, which is shown to be essential for predicting the effects on performance of the feedback between temperature and current inside the highly anisotropic cell. Different material properties for current collectors and electrodes are included in the jellyroll in both the electrical and thermal model. It is shown that including the cell metal can on top of the usually studied jellyroll is crucial to obtaining trustworthy predictions of the combined effect of cooling approaches and number of cell tabs. The model is coded in Python and allows a high degree of cell customization, including number and position of tabs and level of discretization. The model is parametrized and validated from bespoke experiments on LG M50T cells, including experiments on cells instrumented with internal thermocouples.

Model predictions are compared to those of a corresponding lumped thermally coupled ECN model. The lumped model's failure to allow for inhomogeneity of temperature, state of charge and current density inside the cell has a substantial impact on model accuracy, making it a poor predictor of cell behavior.

The distributed model was used to investigate the effectiveness of different thermal management strategies and the effect of cell designs with different tab configurations, by introducing two figures of merit that describe the ability to maintain low average temperature and low thermal gradients within a cell. The results showed that a cell design with multiple tabs and side conductive cooling provided the best cooling and minimized internal thermal inhomogeneities. Increasing the number of tabs beyond one per current collector can reduce the internal inhomogeneities by 25.41%, by providing more uniform current densities in the cell, and thus more uniform heat generation and temperature. Side conductive cooling is more effective than base conductive cooling at removing heat due to the increased cooling surface, but both create similar thermal gradients for a given tab design.

The modelling framework and results presented here should be of immediate interest to both cell manufacturers, module and pack designers, as they present a tool to optimize cell manufacturing, cell selection, and cooling approach for system-level performance.

Acknowledgements

We thankfully acknowledge Dr. Yan Zhao for technical support in modelling.

This work was supported by the Faraday Institution (grant no. EP/S003053/1,

FIRG003), the Innovate UK BATMAN project (grant no. 104180), the Innovate UK WIZer project (grant no. 104427), and the UK EPSRC TRENDs project (grant no. EP/R020973/1).

Nomenclature

Abbreviations	Description
cond	Conduction
conv	Convection
CC	Constant current
CV	Constant voltage
ECN	Equivalent circuit network
GITT	Galvanostatic intermittent titration technique
insu	Insulation
LIB	Lithium-ion battery
MSMD	Multi-scale multi-dimensional
NMC	Nickel Manganese Cobalt oxide
NTGK	Semi-empirical model named by Newman, Tiedemann, Gu and Kwon
OCV	Open circuit voltage
PID	Proportional-integral-derivative
PTFE	Polytetrafluoroethylene
P2D	Pseudo two-dimensional
RC	Resistor-capacitor pair
RMSE	Root mean square error
SD	Standard deviation
SEM	Scanning electron microscope
SoC	State of charge
TC	Thermocouple
TMS	Thermal management system

Latin symbols	Unit	Description
c	$J \cdot kg^{-1} \cdot K^{-1}$	Specific heat capacity
E_s	V	Voltage source
h	$W \cdot m^{-2} \cdot K^{-1}$	Convective heat transfer coefficient
I	A	Total current for electrodes in an electrical ECN element
I_i	A	Branch current for electrodes in an electrical ECN element
I_i^{CC}	A	Constituent current for current collector in an ECN element
q	$W \cdot m^{-3}$	Heat source in a thermal ECN element
q^{CC}	$W \cdot m^{-3}$	Current collector heat generation rate per unit volume
q^{El}	$W \cdot m^{-3}$	Electrodes heat generation rate per unit volume
Q_{conv}	$W \cdot m^{-2}$	Heat transferred by convection
R_0	Ω	Series resistance of one electrical ECN element
R_i	Ω	Branch resistance of one electrical ECN element
R_i^{CC}	Ω	Current collector resistance
S_1	K·s	Average temperature integral over time
S_2	K·s	Temperature standard deviation integral over time
t	s	Time
ΔT_{avg}	K	Metric to gauge cell overall cooling rate
ΔT_{SD}	K	Metric to gauge cell temperature non-uniformity
$T_{ambient}$	K	Surrounding temperature for convective heat transfer
T_{avg}	K	Weighted average temperature

T_{target}	K	Target temperature for cooling strategy
T_{SD}	K	Temperature standard deviation
V_e^{CC}	m^3	Current collector foil volume
V^{El}	m^3	Volume of electrodes
x	m	Spatial coordinate along angular direction
y	m	Spatial coordinate along axial direction
z	m	Spatial coordinate along radial direction

Greek symbols	Unit	Description
δ^{Al}	m	Aluminum foil thickness
δ^{Cu}	m	Copper foil thickness
δ^{El}	m	Electrode pair layer thickness
ϕ^{CC}	V	Electric potential of current collector
ϕ^{El}	V	Terminal voltage of electrodes
λ	$W \cdot m^{-1} \cdot K^{-1}$	Thermal conductivity
λ_x	$W \cdot m^{-1} \cdot K^{-1}$	Thermal conductivity in angular direction
λ_y	$W \cdot m^{-1} \cdot K^{-1}$	Thermal conductivity in axial direction
λ_z	$W \cdot m^{-1} \cdot K^{-1}$	Thermal conductivity in radial direction
ρ	$kg \cdot m^{-3}$	Density
σ	$S \cdot m^{-1}$	Electrical conductivity

Subscripts	Description
avg	Average
conv	Heat convection
eq	equivalent
SD	Standard deviation

Superscripts	Description
Al	Aluminum foil
Cu	Copper foil

El	Electrodes including anode, cathode and separator

References

[1] International Energy Agency, Global EV Outlook 2020. https://www.oecd-ilibrary.org/energy/global-ev-outlook-2020_d394399e-en/, 2020 (accessed 5 January 2021).

[2] C. McKerracher, Electric Vehicle Outlook 2020. https://about.bnef.com/electric-vehicle-outlook/, 2020 (accessed 5 January 2021).

[3] M. Li, J. Lu, Z. Chen, K. Amine, 30 Years of Lithium-Ion Batteries, Adv. Mater. 30 (2018) 1–24.

[4] Z. Lei, C. Zhang, J. Li, G. Fan, Z. Lin, Preheating method of lithium-ion batteries in an electric vehicle, J. Mod. Power Syst. Clean Energy. 3 (2015) 289–296.

[5] B. Wu, V. Yufit, M. Marinescu, G.J. Offer, R.F. Martinez-Botas, N.P. Brandon, Coupled thermal-electrochemical modelling of uneven heat generation in lithium-ion battery packs, J. Power Sources. 243 (2013) 544–554.

[6] X. Feng, X. He, M. Ouyang, L. Lu, P. Wu, C. Kulp, S. Prasser, Thermal runaway propagation model for designing a safer battery pack with 25Ah LiNixCoyMnzO2 large format lithium ion battery, Appl. Energy. 154 (2015) 74–91.

[7] Y. Zhao, Y. Patel, I.A. Hunt, K.M. Kareh, A.A. Holland, C. Korte, J.P. Dear, Y. Yue, G.J. Offer, Preventing lithium ion battery failure during high temperatures by externally applied compression, J. Energy Storage. 13 (2017) 296–303.

[8] C.G. Motloch, J.P. Christophersen, J.R. Belt, R.B. Wright, G.L. Hunt, R.A. Sutula, T. Duong, T.J. Tartamella, H.J. Haskins, T.J. Miller, High-Power Battery Testing Procedures and Analytical Methodologies for HEV's, in: SAE Tech. Pap., SAE International, 2002.

[9] N. Nieto, L. Díaz, J. Gastelurrutia, F. Blanco, J.C. Ramos, A. Rivas, Novel thermal management system design methodology for power lithium-ion battery,

J. Power Sources. 272 (2014) 291–302.

[10] I.A. Hunt, Y. Zhao, Y. Patel, J. Offer, Surface Cooling Causes Accelerated Degradation Compared to Tab Cooling for Lithium-Ion Pouch Cells, J. Electrochem. Soc. 163 (2016) A1846–A1852.

[11] J. Sturm, A. Rheinfeld, I. Zilberman, F.B. Spingler, S. Kosch, F. Frie, A. Jossen, Modeling and simulation of inhomogeneities in a 18650 nickel-rich , silicon-graphite lithium-ion cell during fast charging, J. Power Sources. 412 (2019) 204–223.

[12] H. Zhou, K. An, S. Allu, S. Pannala, J. Li, H.Z. Bilheux, S.K. Martha, J. Nanda, Probing Multiscale Transport and Inhomogeneity in a Lithium-Ion Pouch Cell Using in Situ Neutron Methods, ACS Energy Lett. 1 (2016) 981–986.

[13] H. Inomata, Y. Takahashi, D. Takamatsu, A. Kumatani, H. Ida, H. Shiku, T. Matsue, Visualization of inhomogeneous current distribution on ZrO2-coated LiCoO2 thin-film electrodes using scanning electrochemical cell microscopy, Chem. Commun. 55 (2019) 545–548.

[14] W. Ai, L. Kraft, J. Sturm, A. Jossen, B. Wu, Electrochemical Thermal-Mechanical Modelling of Stress Inhomogeneity in Lithium-Ion Pouch Cells, J. Electrochem. Soc. 167 (2020) 013512.

[15] S. Müller, J. Eller, M. Ebner, C. Burns, J. Dahn, V. Wood, Quantifying Inhomogeneity of Lithium Ion Battery Electrodes and Its Influence on Electrochemical Performance, J. Electrochem. Soc. 165 (2018) A339–A344.

[16] T. Sasaki, C. Villevieille, Y. Takeuchi, P. Novák, Understanding Inhomogeneous Reactions in Li-Ion Batteries: Operando Synchrotron X-Ray Diffraction on Two-Layer Electrodes, Adv. Sci. 2 (2015) 2–7.

[17] T. Waldmann, G. Geramifard, M. Wohlfahrt-Mehrens, Influence of current collecting tab design on thermal and electrochemical performance of cylindrical Lithium-ion cells during high current discharge, J. Energy Storage. 5 (2016) 163–168.

[18] H. Park, A design of air flow configuration for cooling lithium ion battery in hybrid electric vehicles, J. Power Sources. 239 (2013) 30–36.

[19] S. Panchal, K. Gudlanarva, M.K. Tran, R. Fraser, M. Fowler, High reynold's number turbulent model for micro-channel cold plate using reverse engineering approach for water-cooled battery in electric vehicles, Energies. 13 (2020).

[20] M.S. Patil, J.H. Seo, S. Panchal, M.Y. Lee, Numerical study on sensitivity analysis of factors influencing liquid cooling with double cold-plate for lithium-ion pouch cell, Int. J. Energy Res. (2020) 1–27.

[21] N. Yang, X. Zhang, G. Li, D. Hua, Assessment of the forced air-cooling performance for cylindrical lithium-ion battery packs: A comparative analysis between aligned and staggered cell arrangements, Appl. Therm. Eng. 80 (2015) 55–65.

[22] S. Panchal, S. Mathewson, R. Fraser, R. Culham, M. Fowler, Thermal Management of Lithium-Ion Pouch Cell with Indirect Liquid Cooling using Dual Cold Plates Approach, SAE Int. J. Altern. Powertrains. 4 (2015) 293–307.

[23] Y. Zhao, L.B. Diaz, G.J. Offer, How to Cool Lithium Ion Batteries : Optimising Cell Design using a Thermally Coupled Model, 166 (2019) 2849–2859.

[24] S. V. Erhard, P.J. Osswald, J. Wilhelm, A. Rheinfeld, S. Kosch, A. Jossen, Simulation and Measurement of Local Potentials of Modified Commercial Cylindrical Cells, J. Electrochem. Soc. 162 (2015) A2707–A2719.

[25] K.J. Lee, K. Smith, A. Pesaran, G.H. Kim, Three dimensional thermal-, electrical-, and electrochemical-coupled model for cylindrical wound large format lithium-ion batteries, J. Power Sources. 241 (2013) 20–32.

[26] X. Cheng, T. Li, Y. Tang, S. Wang, Influences of structure components on thermal distribution of a cylindrical lithium-ion battery, Energy Procedia. 158 (2019) 4959–4966.

[27] Y. Zhao, Y. Patel, T. Zhang, G.J. Offer, Modeling the Effects of Thermal Gradients Induced by Tab and Surface Cooling on Lithium Ion Cell Performance, J. Electrochem. Soc. 165 (2018) A3169–A3178.

[28] K. Tsuruta, M.E. Dermer, R. Dhiman, Cell with a tabless electrode, 16/673464, 2020. https://patents.google.com/patent/US20200144676A1/en/ (accessed 5 January 2021)

[29] M. Doyle, T.F. Fuller, J. Newman, Modeling of Galvanostatic Charge and Discharge of the Lithium Polymer Insertion Cell, J. Electrochem. Soc. 140 (1993) 1526–1533.

[30] K. Smith, C.Y. Wang, Power and thermal characterization of a lithium-ion battery pack for hybrid-electric vehicles, J. Power Sources. 160 (2006) 662–673.

[31] K. Kumaresan, G. Sikha, R.E. White, Thermal Model for a Li-Ion Cell, J. Electrochem. Soc. 155 (2008) A164.

[32] A. Jokar, B. Rajabloo, M. Désilets, M. Lacroix, Review of simplified Pseudo-two-Dimensional models of lithium-ion batteries, J. Power Sources. 327 (2016) 44–55.

[33] G.-H. Kim, K. Smith, K.-J. Lee, S. Santhanagopalan, A. Pesaran, Multi-Domain Modeling of Lithium-Ion Batteries Encompassing Multi-Physics in Varied Length Scales, J. Electrochem. Soc. 158 (2011).

[34] M. Haug, A. Noel, J. Wilhelm, T. Thoennessen, A. Rheinfeld, A. Jossen, Simulation and Measurement of the Current Density Distribution in Lithium-Ion Batteries by a Multi-Tab Cell Approach, 164 (2017) 6324–6333.

[35] B. Rieger, S. V Erhard, S. Kosch, M. Venator, A. Rheinfeld, A. Jossen, Multi-Dimensional Modeling of the Influence of Cell Design on Temperature , Displacement and Stress Inhomogeneity in Large-Format Lithium-Ion Cells, 163 (2016).

[36] S. Kosch, Y. Zhao, J. Sturm, G. Mulder, E. Ayerbe, A. Jossen, A Computationally Efficient Multi-Scale Model for Lithium-Ion Cells, 165 (2018) 2374–2388.

[37] S. Panchal, M. Mathew, R. Fraser, M. Fowler, Electrochemical thermal modeling and experimental measurements of 18650 cylindrical lithium-ion battery during discharge cycle for an EV, Appl. Therm. Eng. 135 (2018) 123–132.

[38] J. Newman, W. Tiedemann, Porous‐electrode theory with battery applications, AIChE J. 21 (1975) 25–41.

[39] H. Gu, Mathematical-Analysis of a Zn/Niooh Cell, J. Electrochem. Soc. 130 (1983) 1459–1464.

[40] K.H. Kwon, C.B. Shin, T.H. Kang, C.-S. Kim, A two-dimensional modeling of

a lithium-polymer battery, J. Power Sources. 163 (2006) 151–157.

[41] U.S. Kim, C.B. Shin, C.-S. Kim, Effect of electrode configuration on the thermal behavior of a lithium-polymer battery, J. Power Sources. 180 (2008) 909–916.

[42] H. Soltanali, A. Rohani, M. Tabasizadeh, M.H.A.- Fard, A. Parida, International Journal of Automotive, Int. J. Automot. Eng. 8 (2018) 2781–2791.

[43] S.S. Madani, M. Swierczynski, S.K. Kær, Cooling Simulation and Thermal Abuse Modeling of Lithium-Ion Batteries Using the Newman, Tiedemann, Gu, and Kim (NTGK) Model, ECS Trans. 81 (2017) 261–270.

[44] Y. Liu, Y.G. Liao, M.-C. Lai, Transient Temperature Distributions on Lithium-Ion Polymer SLI Battery, Vehicles. 1 (2019) 127–137.

[45] C. Veth, D. Dragicevic, R. Pfister, S. Arakkan, C. Merten, 3D Electro-Thermal Model Approach for the Prediction of Internal State Values in Large-Format Lithium Ion Cells and Its Validation, J. Electrochem. Soc. 161 (2014) A1943–A1952.

[46] D. Chen, J. Jiang, X. Li, Z. Wang, W. Zhang, Modeling of a pouch lithium ion battery using a distributed parameter equivalent circuit for internal non-uniformity analysis, Energies. 9 (2016).

[47] R. O'Hayre, S.-W. Cha, W. Colella, F. Prinz, Fuel Cell Fundamentals, Wiley, 2016.

[48] T. Bergman, L. Adrienne, F. Incropera, D. DeWitt, F Fundamentals of Heat and Mass Transfer, eighth edi., Wiley, 2017.

[49] C.-H. Chen, F. Brosa Planella, K. O'Regan, D. Gastol, W.D. Widanage, E. Kendrick, Development of Experimental Techniques for Parameterization of Multi-scale Lithium-ion Battery Models, J. Electrochem. Soc. 167 (2020) 080534.

[50] A. Hales, L.B. Diaz, M.W. Marzook, Y. Patel, G. Offer, The Cell Cooling Coefficient : A Standard to Define Heat Rejection from Lithium-Ion Batteries, 166 (2019) 2383–2395.

[51] J. Fleming, T. Amietszajew, J. Charmet, A.J. Roberts, D. Greenwood, R. Bhagat, The design and impact of in-situ and operando thermal sensing for smart energy

storage, J. Energy Storage. 22 (2019) 36–43.

[52] T. Amietszajew, J. Fleming, A.J. Roberts, W.D. Widanage, D. Greenwood, M.D.R. Kok, M. Pham, D.J.L. Brett, P.R. Shearing, R. Bhagat, Hybrid Thermo‐Electrochemical In Situ Instrumentation for Lithium-Ion Energy Storage, Batter. Supercaps. 2 (2019) 934‐940.

[53] D.A.H. McCleary, J.P. Meyers, B. Kim, Three-Dimensional Modeling of Electrochemical Performance and Heat Generation of Spirally and Prismatically Wound Lithium-Ion Batteries, J. Electrochem. Soc. 160 (2013) A1931–A1943.

[54] R.R. Richardson, S. Zhao, D.A. Howey, On-board monitoring of 2-D spatially-resolved temperatures in cylindrical lithium-ion batteries: Part I. Low-order thermal modelling, J. Power Sources. 326 (2016) 377–388.

[55] M. Fleckenstein, O. Bohlen, M.A. Roscher, B. Bäker, Current density and state of charge inhomogeneities in Li-ion battery cells with LiFePO4as cathode material due to temperature gradients, J. Power Sources. 196 (2011) 4769–4778.

[56] V. Vishwakarma, C. Waghela, Z. Wei, R. Prasher, S.C. Nagpure, J. Li, F. Liu, C. Daniel, A. Jain, Heat transfer enhancement in a lithium-ion cell through improved material-level thermal transport, J. Power Sources. 300 (2015) 123–131.

[57] J.V. Barreras, C. Fleischer, A.E. Christensen, M. Swierczynski, E. Schaltz, S.J. Andreasen, D.U. Sauer, An Advanced HIL Simulation Battery Model for Battery Management System Testing, IEEE Trans. Ind. Appl. 52 (2016) 5086–5099.

[58] K.J. Lee, K. Smith, A. Pesaran, G.H. Kim, Three dimensional thermal-, electrical-, and electrochemical-coupled model for cylindrical wound large format lithium-ion batteries, J. Power Sources. 241 (2013) 20–32.

[59] X.Y. Yao, M.G. Pecht, Tab design and failures in cylindrical li-ion batteries, IEEE Access. 7 (2019) 24082–24095.